Fatigue behavior of vacuum-sintered binder jetted fine 316L stainless steel powder

Mohammad Jamalkhani a, Bradley Nathan a, Mike Heim b, Dave Nelson b, Amir Mostafaei a,*

- $^{\rm a}$ Department of Mechanical, Materials, and Aerospace Engineering, Illinois Institute of Technology, 10 W $32^{\rm nd}$ Street, Chicago, IL 60616, USA
- ^b Nel Pretech Corporation, 8420 183rd Place, Tinley Park, IL 60487, USA
- * Corresponding author: A. Mostafaei (<u>mostafaei@iit.edu</u>)

Abstract

The study examined the impact of surface roughness on the high-cycle fatigue (HCF) properties of vacuum-sintered binder jetted gas atomized fine 316L stainless steel (SS) powder. The microstructure and density of the as-sintered specimens were analyzed using micro-computed tomography, indicating a relative density of ~99.8±0.1% with equiaxed grains surrounded by delta-ferrite phase at the grain boundaries (volume fraction of $\sim 2\%$). The as-sintered specimens had a rough surface with an arithmetical mean roughness of R_a =6.56±0.58 µm and root-mean-square roughness of R_a =8.29±0.68 µm. After mechanical grinding, the surface roughness was reduced to R_a =0.21±0.03 µm and R_a =0.25±0.04 µm. Microhardness analysis revealed an increase of nearly 70% up to 125 μm beneath the surface of mechanically ground specimens. The enhanced surface hardness was found to be related to an in-plane compressive residual stress on the mechanically ground sample. The fatigue endurance limit was evaluated using the staircase test methodology, with an average value of ~170 and 225 MPa for the as-sintered and mechanically ground parts, respectively. Highcycle fatigue experiments were conducted at a stress ratio of R_{σ} =-1, and the results showed that surface grinding improved fatigue life at higher stress levels due to in-plane compressive stress and the reduction in surface roughness. Fractography revealed that the fracture mechanisms in the crack propagation and final fracture zones were striation marks and dimple features. Finally, the electron backscatter diffraction technique was used to study the deformation history at different sites close to the fracture surface.

Keywords: Additive manufacturing; High-cycle fatigue; Fatigue endurance limit; Surface roughness; Computed tomography; Fractography.

1. Introduction

Binder Jetting is among the seven Additive Manufacturing (AM) techniques listed in the ISO/ASTM 52900:2021 [1]. It consists of the layer-by-layer selective deposition of a liquid bonding agent on a powder bed, obtained by the spreading of a particulate feedstock on the building platform, followed by a series of post-processing procedures aimed at consolidating and densifying the printed components [2]. In the past few years, the near-net shaping capabilities of binder jetting, diverse metal powder choice, and supersolidus liquid phase sintering (SLPS) brought attention to research and industry sectors for manufacturing metallic components using this non-beam-based AM [3–5]. Furthermore, a faster production rate via binder jetting and minimization of cracks during consolidation have made such an AM technique an attractive manufacturing process for metal 3D printing [6,7].

The majority of research on binder jetting of metal powder has been focusing on process development and densification to attain parts with a relative density of >98% [8-17]. A few pieces of literature studied tensile strength and ductility [8,10,18-23] and reported that the strength was typically lower than the wrought alloys due to the grain coarsening and remnant pores in the final microstructure of binder jetted sintered parts. In an effort to characterize the effect of surface finish on the fatigue properties of the binder jetted 625 alloy, Mostafaei et al. [24] found that the as-sintered parts had lower fatigue performance compared to cast parts while the mechanically ground specimens showed superior fatigue properties related to the reduced surface roughness and the induced compressive residual stress after surface grinding. Kumar et al. [20,25] studied the fatigue behavior of the binder jetted stainless steel alloys under rotating-bending loading conditions. They reported that the microstructure of the binder jetted 316L SS with a final relative density of 95±1% consisted of austenitic grain with annealing twins as well as delta-ferrite at the grain boundaries. Regarding the fatigue life, they showed that the high fraction of porosity (up to 6%) did not adversely impact the high-cycle fatigue (HCF) since the fatigue cracks remained short and controlled by microstructure. Kimes et al. [26] found that the high surface roughness and presence of inclusions negated the benefits of hot isostatic pressing (HIP) on the microstructure; thus, no difference in the fatigue life of the as-sintered and HIPed specimens was reported. Muhammad et al. [27] demonstrated when primitive in-layer line defects remain in the microstructure of the sintered parts, elongated pores could form after sintering and act as a crack initiation site under fatigue loading.

There is a lack of experimental research on the fatigue performance of near fully dense parts manufactured by binder jetting followed by sintering. In the previous study [28], a thorough investigations were carried out on densification, grain structure and pore evolution in the sintered 316L SS specimens. Use of fine binder jetted powder could lower surface roughness of the as-sintered specimens, enhance thermodynamic of sintering, and result in find grain structure in final production [9,29]. Although extensive research has been conducted on fatigue behavior of fusion-based additively manufactured 316L SS, the available literature on fatigue life of binder jetted 316L SS is limited. Hence, by considering the roles of microstructure and remnant porosity on the mechanical properties of the binder jetted 316L SS, this research aimed to study the influence of surface roughness on the HCF and fatigue endurance limit of the vacuum-sintered binder jetted fine 316L SS part under fully-reversed axial loading condition.

2. Materials and Methods

2.1. Feedstock

In this study, gas atomized 316L SS powder with spherical morphology was purchased from Sandvik Osprey Company with a chemical composition of Cr=18.28 wt.%, Ni=10.9 wt.%, Mo=2.12 wt.%, C=0.03 wt.%, Si=0.58 wt.%, Mn=2.19 wt.%, and Fe=balance. The particle size distribution (PSD) analysis was conducted using a Beckman Coulter LS13 320XR Analyzer with the Tornado Dry Powder System, and the result was given in Figure 1 (A). Powder morphology was observed using an electron microscope (SEM, model JEOL 5900LV) and micrograph was shown in Figure 1 (B).

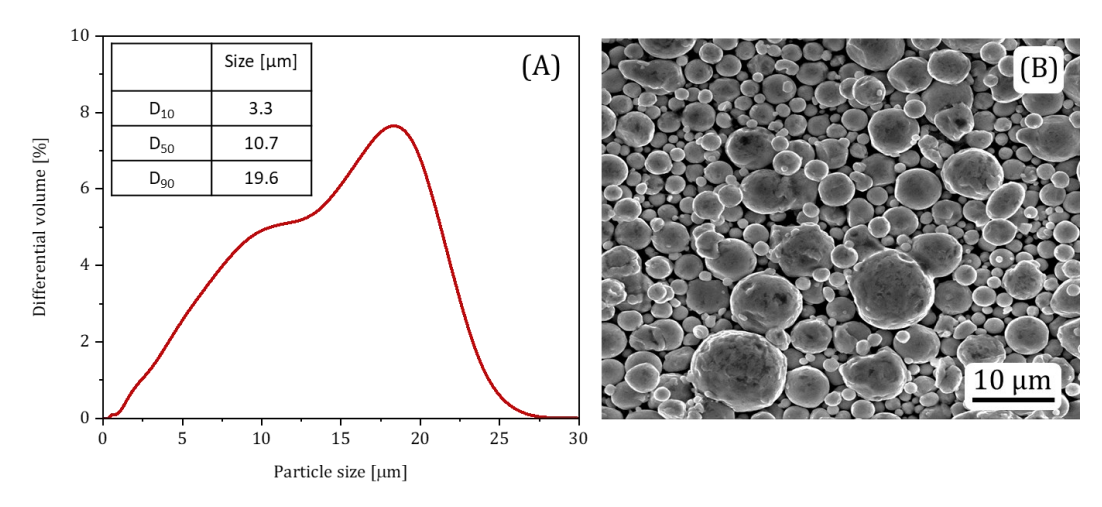


Figure 1. (A) Particle size versus the differential volume and (B) powder morphology of the fine gas atomized 316L SS powder. The inset in (A) summarizes the PSD results.

2.2. Processes

2.2.1. Binder jetting

Figure 2(A) showed schematic of the fatigue specimen's geometry with a circular cross-section and a continuous radius between ends based on ASTM E466. Parts were manufactured using an ExOne Innovent+ binder jet printer with the process parameters including Layer thickness of 50 μ m, Binder saturation of 80% (detailed information can be found in [28]). Samples were printed horizontally (y-oriented) in the build box with a layout shown in Figure 2 (B). An AquaFuse water-based binder (BA-005 solution supplied by the ExOne Company) was used for the binder jetting process. The printed parts were cured in an oven at 185±2 °C for 8 h followed by depowdering using a brush, and the recycled powder was reused to print specimens.

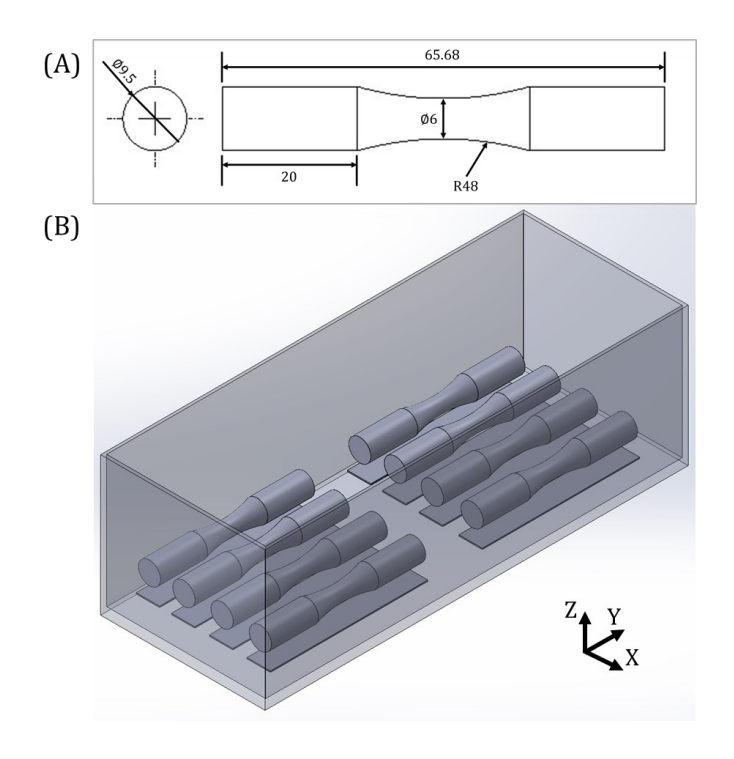


Figure 2. (A) Dimension of the designed fatigue samples and (B) schematic of the designed layout of the fatigue samples. Support structure (*aka* setter) was added beneath each sample to minimize cracking in the gage area.

2.2.2. Sintering

To achieve desired relative density of >99%, sintering was conducted under vacuum conditions ($\sim 10^{-5}$ bar) in an Across International FT1700 tube furnace. To minimize deformation in final sintered specimens, fatigue samples were sintered in a bed of alumina powder. In the sintering profile, a debinding stage was considered at 600 °C with a dwell time of 1 h. The maximum sintering temperature of 1400 °C with a dwell time of 2 h and a heating rate of 5 °C/min was selected to ensure the SLPS takes place [28].

2.3. Characterization

The pores' spatial arrangement was observed using a ZEISS Metrotom 800 X-ray microcomputed tomography (μ -CT) machine. The X-ray energy and current used were 130 kV and 47 mA, respectively, with an Al 2.0 mm filter. The frames were averaged four times, and the angular range was 360° with a step size of 0.12°, which resulted in a spatial resolution of 5.02

μm/pixel. Afterward, the data was reconstructed and analyzed using Volume Graphics Studio Max 3.5.1.

To analyze the microstructure of the fatigue specimen, it was first sectioned on the XZ plane and then hot mounted with MetLab phenolic thermosetting molding powder. The mounted sample was then ground using SiC sandpapers up to P4000, and polished using 3 μm diamond abrasive and 1 μm and 0.05 μm Al203 abrasive. The final polishing step involved using 0.04 μm colloidal silica and a platen grinder-polisher machine (Buehler Phoenix 4000). The microstructure and texture were analyzed using a scanning electron microscope (model JEOL 5900LV) equipped with an Oxford Instruments electron backscatter diffraction (EBSD) detector. The microscope was operated at an acceleration voltage of 20 keV, and the step size was set to 0.7 μm . The HKL Channel 5 software package was used to analyze the obtained EBSD data.

The specimens were subjected to fatigue tests with two different surface finish conditions: as-sintered and mechanically ground. To achieve a smoother surface, a rotary tool (Dremel 4000, Dremel, Racine, Wisconsin, USA) was utilized, followed by grinding with 400, 600, 800, and 1200 grit SiC sandpapers. Surface roughness measurements were taken along multiple directions on the test volumes using a Keyence digital microscope (model VHX-7100) to ensure quality and consistency. Stress-controlled high-cycle fatigue experiments were performed on an MTS 800 machine with uniaxial sinusoidal cyclic loading and a stress ratio of $R_{\sigma}=-1$. The applied stress levels and test frequencies ranged between 125-325 MPa and 5-15 Hz, respectively. Three specimens were tested at each stress level, with a run-out test limit of 2×10^6 cycles [30]. Additionally, the fatigue endurance limit was determined using the staircase test methodology, and ten specimens were tested for each surface condition. The starting stress level for this test methodology was based on the HCF results in the finite life region, and the stress increment was set at 25 MPa.

To assess the extent of sub-surface deformation and induced stress caused by mechanical grinding, microhardness testing was carried out on cross-sections of the fatigue samples. The as-sintered and mechanically ground specimens were sectioned using a wire electric discharge machine (Mitsubishi FX10k Wire-EDM machine). The cross-section surfaces were ground using 400-1200 grit SiC sandpapers. Afterward, the Vickers

microhardness test was carried out on the prepared surfaces using a Buehler model Micromet 2 microhardness tester under 50 gf loads with a dwell time of 15 s. Two replicates were performed per sample. An X-ray diffractometer (XRD, model Thermo ARL) was used with Cu–K α radiation (λ = 1.54 Å, 35 kV, 30 mA) with a step of 0.02°, a scan speed of 1 s/step, and 2 θ ranging from 45° to 100° at room temperature to analyze residual stress on the surface of specimens.

Finally, fractography was performed on the fracture surfaces using Keyence optical microscope and field-emission scanning electron microscope (FESEM, model JEOL JSM-6701F). To assess the strain history in the fractured region, samples were sectioned perpendicular to the fracture surface and prepared for EBSD observation followed by the sample preparation procedure indicated in section 2.3.

3. Results and discussions

3.1. Microstructure and porosity analysis

The grain structure and residual pores have a significant impact on the mechanical properties of additively manufactured components. Figure 3 A-C illustrate that the final microstructure of the as-sintered 316L SS alloy consists of austenite grains with annealing twins, as well as delta-ferrite at the grain boundaries. An earlier study [28] found that the burnout step increased the C content from ~ 0.025 wt% in the feedstock to 0.135 wt%. This increase lowered the solidus temperature to 1366 °C, enabling SLPS to occur at 1400 °C. The C content in the final sintered samples decreased to ~ 0.027 wt.%. Elemental and phase analysis using EDS and EBSD techniques confirmed the presence of delta-ferrite ($\sim 2\%$) and trace amounts of sigma phase enriched in Fr-Cr-Mo at the grain boundaries, which has a bct crystalline structure, consistent with previous studies [20,31–34]. Figure 3D depicts the 3D and 2D projections of the as-sintered binder jetted 316L SS, as visualized by μ -CT. Porosity analysis indicated a relative density of 99.8% with a uniform distribution of porosity. Most of the pores had an equivalent diameter between 20-40 μ m, highlighting the importance of μ -CT in the visualization and measurement of porosity in binder jetted parts.

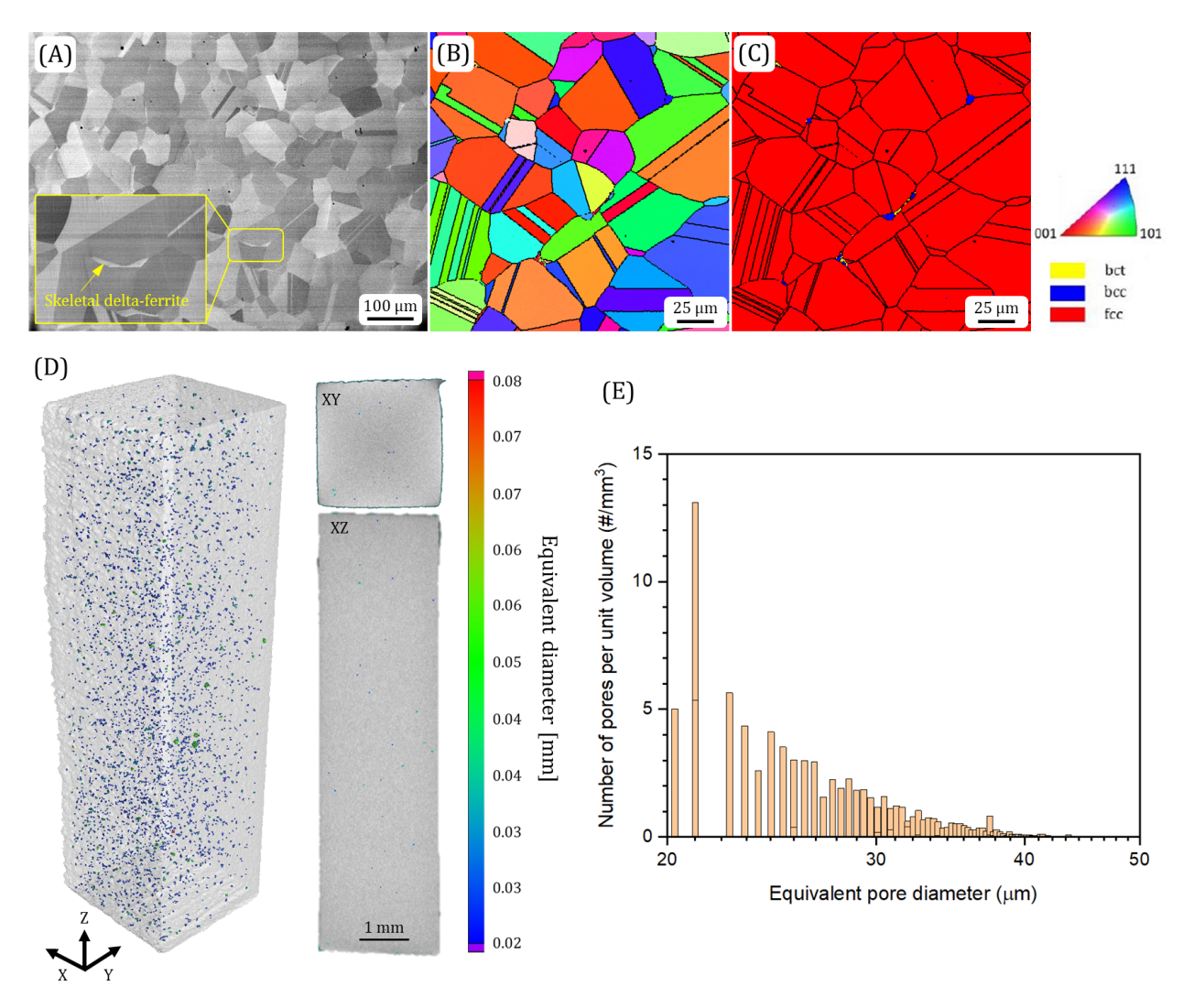


Figure 3. (A) Scanning electron micrographs, (B) inverse pole figure (IPFY), and (C) phase map results of the binder jetted 316L SS alloy sintered at the temperature of 1400 °C for 2hrs. In (C), Red areas are austenitic grains, blue regions at the grain boundaries are delta-ferrite, and yellow spots are sigma phase. (D) μ -CT results in 3D and 2D shadow projections. The color bar showed the equivalent pore diameter in mm. (E) Normalized porosity count in 1 mm³. The effective volume of the μ -CT specimen was 37.7 mm³.

3.2. Surface roughness analysis

Before conducting fatigue tests, the surface topography and roughness of the assintered and mechanically ground conditions were analyzed. Figure 4 (top row) shows optical micrographs of the curved surface of the fatigue specimens in both conditions. The as-sintered specimen had a layer-wise printing pattern of metal powders stacked on top of each other, resulting in deep valleys on the surface and increased surface roughness. The surface roughness was measured before and after surface grinding using optical

profilometry, and the results are displayed in Figure 4 (middle and bottom rows). The heat map of the surface roughness showed that the binder droplet and its ejections played a significant role in creating extreme roughness peaks and valleys. To quantify surface roughness, the arithmetical mean roughness (R_a) and root-mean-square deviation (R_q) were measured using the following equations in accordance with ISO 4288:

$$R_a = \frac{1}{l} \int_0^l |Z(x)| \, dx \approx \frac{1}{n} \sum_{i=1}^n |Z_i| \tag{1}$$

$$R_{q} = \sqrt{\frac{1}{l} \int_{0}^{l} Z^{2}(x) dx} \approx \sqrt{\frac{1}{n} \sum_{i=1}^{n} Z_{i}^{2}}$$
 (2)

where l is the reference length, n is the number of discrete profile deviations, and Z(x) takes the average height of the roughness profile to be zero and determines the height of position x along the curve.

The calculated roughness values were given in

Table 1. Results showed that after the sintering process, the roughness values decreased from $R_a=9.48\pm1.85~\mu m$ and $R_q=11.93\pm2.13~\mu m$ in the as-printed condition to $R_a=6.56\pm0.58~\mu m$ and $R_q=8.29\pm0.68~\mu m$ in the as-sintered specimen. After mechanical grinding, surface roughness drastically decreased to $R_a=0.21\pm0.03~\mu m$ and $R_q=0.25\pm0.04~\mu m$. Typically, R_q is more sensitive to peak and valley than R_a since the square of height values were considered for the roughness measurement in the former one. Mostafaei et al. [24] showed that the binder jetted 625 alloy using feedstock with PSD of 15-53 μ m resulted in roughness values of $R_a=7.65\pm1.58~\mu m$ and $R_q=12.01\pm2.52~\mu m$ in the as-sintered condition while the roughness decreased to $R_a=1.45\pm0.49~\mu m$ and $R_q=2.78\pm1.10~\mu m$ after mechanical grinding. Such higher surface roughness values could be the consequence of using feedstock with higher PSD compared to the fine powder (<22 μ m) utilized in the current study.

As the initiation of cracks mostly determines the fatigue life, surface roughness plays a vital role, especially at low stress amplitudes [35]. Even though the ultimate tensile strength

and fatigue performance of L-PBF processed parts are usually superior to those of assintered binder jetted parts (in the limited lifetime region), the greater surface roughness leads to almost identical performance at low stress levels, especially in the fatigue endurance limit zone. These details will be further explained in section 3.2.

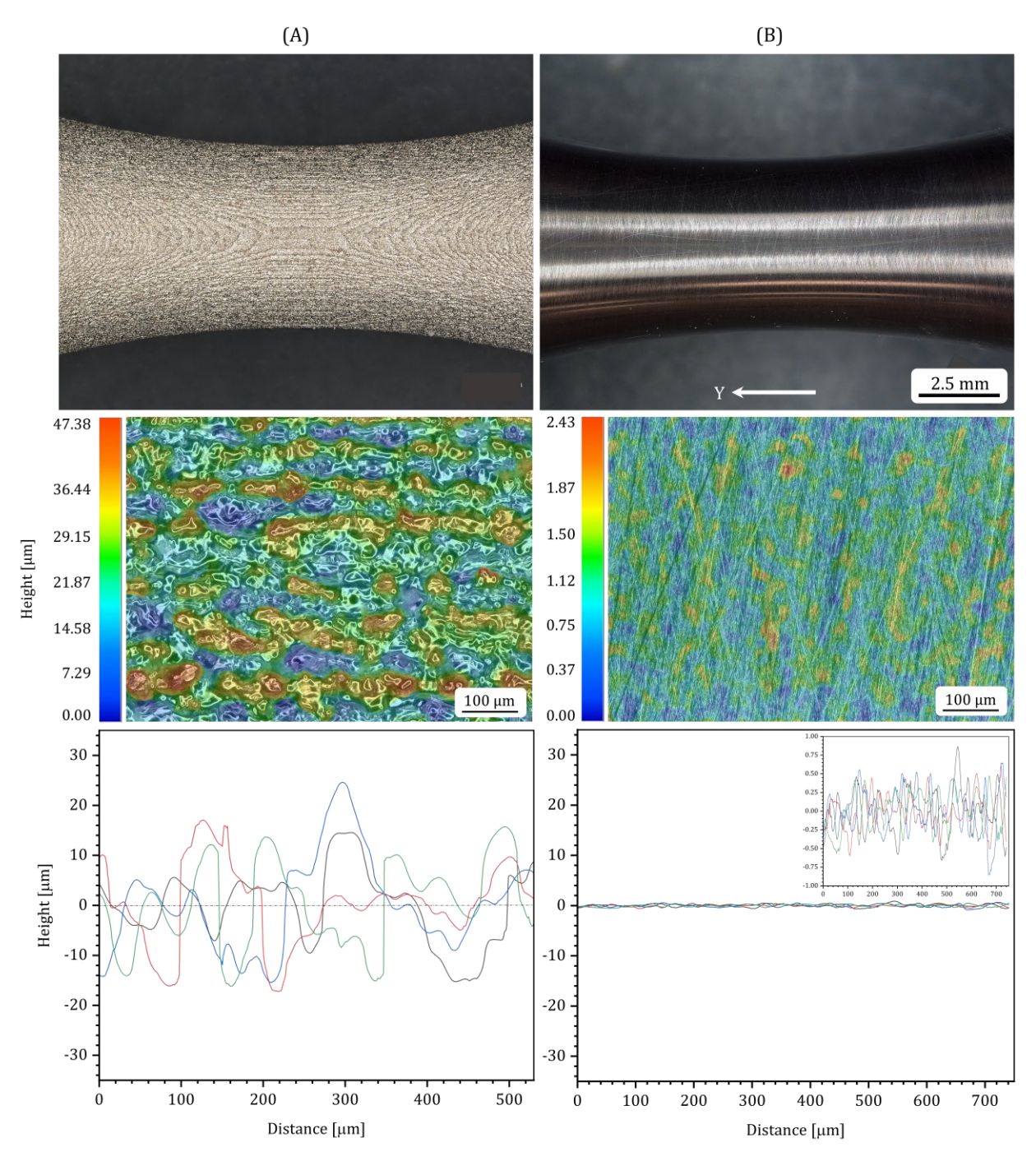


Figure 4. (Top row) Optical image of the test section, (Middle row) optical surface topography micrograph, and (Bottom row) surface roughness profile of the (A) as-sintered and (B) mechanically ground fatigue specimens.

Table 1. The calculated arithmetical mean roughness and root-mean-square roughness values of different surface conditions.

Sample	R _a [μm]	R _q [μm]	
As-printed	9.48 ± 1.85	11.93 ± 2.13	
As-sintered	6.56 ± 0.58	8.29 ± 0.68	
Mechanically ground	0.21 ± 0.03	0.25 ± 0.04	

3.3. Fatigue performance

3.3.1. Stress-lifetime results (S-N curves)

In order to investigate the impact of surface roughness on the fatigue behavior of the binder jetted 316L SS, the specimens in both as-sintered and mechanically ground conditions were tested. The findings are presented in Figure 5, and compared to previously reported data on 316L SS parts produced using other techniques [36–38]. It is important to note that the stress amplitudes in these studies were normalized using the Smith-Watson-Topper equation [39]. The binder jetted 316L SS had a yield strength of approximately 200 MPa and a tensile strength of 574 MPa [28]. Despite the fact that the applied stress range exceeded the yield point, strain hardening facilitated by twining deformation in 316L SS makes it capable of withstanding higher stress levels. In fact, when 316L SS is subjected to stress or strain cycling, inelastic deformation occurs, and the dislocation density increases rapidly. As the dislocation density increases, the mobility of dislocations decreases. Thus, if the movement or glide of dislocations is constrained and minimized, the material undergoes cyclic hardening, resulting in an increase in cyclic yield strength beyond the monotonic yield strength [40].

To characterize the finite lifetime region behavior of the binder jetted 316L SS, Basquin equation was used that was developed from a log-log S-N graph [40,41]:

$$\sigma_a = \sigma_f' (2 N_f)^b \tag{3}$$

where σ_a is the stress amplitude, σ_f' is the fatigue strength coefficient, N_f is the number of cycles to failure, and b is the fatigue strength exponent.

In Figure 5, the S-N curve including all experimental results (the stress amplitude versus the high-cycle fatigue lifetime) with their curve fittings was presented. By the regression analysis, a coefficient of determination (R^2) of >0.95 was obtained for all datasets. Material constants such as σ_f' and b were reported in Table 2 along with R^2 values. The calculated fatigue strength coefficient was $\sigma_f' = 404$ MPa for the as-sintered samples while it increased to 550 MPa in the mechanically ground samples. Also, the computed fatigue strength exponents were b = -0.05 and -0.07 for the as-sintered and mechanically ground parts, respectively, which fell in the typical range of -0.05 to -0.12 for most metals [42].

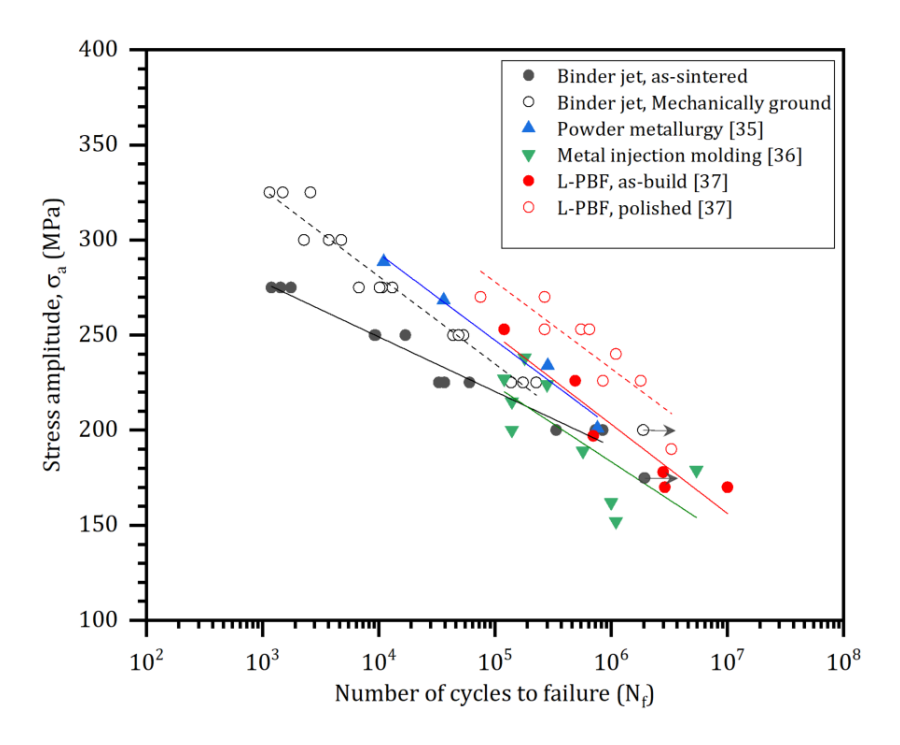


Figure 5. Finite lifetime fatigue data of the binder jetted 316L SS alloy in as-sintered and mechanically ground conditions.

Table 2. Fatigue strength coefficient (σ'_f), fatigue strength exponent (b), and calculated fatigue strength at 1,000 cycles (σ_a) using Basquin equation.

	b	σ_f'	σ_a at 1,000 cycles	R^2	Ref.
As-sintered	-0.053	404.09	270.0993	0.97	This study
Mechanically ground	-0.074	550.47	313.6588	0.96	This study
Powder metallurgy	-0.09	626.35	316.0271	0.57	[36]
Metal injection molding	-0.081	623.68	336.96	0.96	[37]
L-PBF as-build	-0.099	789.15	371.8413	0.91	[38]
L-PBF polished	-0.085	744.89	390.3953	0.75	[38]

The experimental results in Figure 5 showed that the fatigue life decreased with an increase in stress amplitude. In the as-sintered specimens, the values of stress amplitudes between 275-250 MPa yield at 1,189−16,916 cycles while lowering the applied load to 200 MPa showed a much higher fatigue life of 335,530−843,017 cycles. In the mechanically ground specimen, a shorter lifetime was observed at higher values of stress amplitude (275-325 MPa) in which parts ruptured after 1,149-13,061 cycles. In addition, the high-cycle fatigue area was found to be at the stress amplitudes of ≤225 MPa.

Previous studies have reported anisotropy in both microstructure and spatial distribution of pores in binder jetted materials [8,20,27,43,44]. However, these concerns have been reduced by optimizing the process parameters and using advanced compaction technology in binder jet systems [28]. Consolidation and achieving a homogeneous microstructure during the sintering process also depend on factors such as thermal cycles, holding time, and atmosphere. Muhammad et al. [27] studied the densification behavior and fatigue performance of binder jetted 316L SS and found that a minimum green density of >~58% is required to minimize primitive porosity lines that are generated during the printing process. They also observed that the in-layer connected pores in the green state may remain in the microstructure even after sintering, which can be a major cause of crack initiation under fatigue loading. Kimes et al. [26] investigated the effect of post-treatments such as machining and HIPing on the fatigue life of binder jetted 316L SS. They found that the surface roughness on the as-sintered samples and the presence of inclusions nullified the benefits of HIP on the mechanical properties, resulting in no difference in the fatigue life of the as-sintered and HIPed specimens.

Kumar et al. [20] recently investigated the HCF properties of binder jetted 316L SS under rotating-bending loading conditions. Surprisingly, they found that the fatigue performance of the binder jetted 316L SS parts with a relative density of 94-96% was better than that of fusion-based fabricated 316L SS with a relative density of 99.5%. The reported fatigue strength was approximately 250 MPa, which was even higher than the yield strength of 190-200 MPa in 316L SS. Authors hypothesized that the high fatigue strength was due to a combination of planar slip deformation mechanism, high-angle grain boundaries, δ -ferrite phase, and annealing twin boundaries, which prevented the growth of initiated cracks and

postponed crack propagation at the pore during cyclic loading. Although this explanation seems convincing, the high fatigue strength of the binder jetted 316L SS, which was unaffected by the high fraction of pores and low yield strength, still requires further investigation. Stephens et al. [40] justified the higher fatigue performance of parts subjected to rotating-bending loading compared to parts under uniaxial tensile loading for two reasons. Firstly, the entire test section experiences uniform stress in cyclic axial loading, which can lead to inadequate dissipation of hysteresis energy, resulting in an increase in temperature and a decrease in fatigue properties of the specimen. Secondly, there is a higher probability of crack initiation sites in the specimen under axial loading because a larger volume of material is under maximum stress in this specimen compared to the specimen under rotating-bending loading. In other words, the rotating bending fatigue strength is known to be higher than the tension-compression fatigue strength due to the stress gradient.

3.3.2. Endurance limit

To statistically evaluate the fatigue limit properties, the staircase test methodology was utilized among several available techniques. The initial test was conducted at a predetermined stress level of 150 MPa for the as-sintered condition and 200 MPa for the mechanically ground condition. If a failure occurred within the life of interest of 2×10^6 cycles, the next specimen was tested at a lower stress level. Conversely, if no failure was observed, the next test was carried out at a higher stress level. Therefore, the condition of each test was based on the results of its previous experiment. The stress increment was set at 25 MPa, which was consistent with the stress increment of the finite lifetime region tests. Eleven tests were conducted on both surface finish conditions, and the Dixon-Mood data reduction technique was used to determine the statistical parameters of the results. It should be noted that this data reduction technique is obtained through the maximum likelihood estimation method and employs normal distribution for fitting the data [41]. To assess the mean value (μ_S) and standard deviation (σ_S) of the fatigue limit (S_e) , two parameters of A and B should be calculated first:

$$A = \sum_{i} i \times n_i \tag{4}$$

$$B = \sum i^2 \times n_i \tag{5}$$

where i is the number of the stress level (i=0 for the lowest stress level) and n_i is the number of the less frequent event at the numbered stress level i.

Then, μ_S is derived by the following equation:

$$\mu_s = S_0 + d \times \left(\frac{A}{\sum n_i} \pm 0.5\right) \tag{6}$$

where S_0 is the lowest stress level (here, 125 and 200 MPa for the as-sintered and mechanically ground samples, respectively) and d is the stress increment. When the less frequest event is survival, the plus sign is used, and the minus sign is used if the less frequent event is failure. σ_S can also be estimated by:

$$\sigma_{S} = 1.62 \times d \times \left[\frac{B \times \sum n_{i} - A^{2}}{(\sum n_{i})^{2}} + 0.029 \right] \quad \text{if} \quad \frac{B \times \sum n_{i} - A^{2}}{(\sum n_{i})^{2}} \ge 0.3$$
 (7)

or

$$\sigma_S = 0.53 \times d$$
 if $\frac{B \times \sum n_i - A^2}{(\sum n_i)^2} < 0.3.$ (8)

After calculating the mean and standard deviation of the fatigue limit, the upper and lower specification limits (USL and LSL) were obtained using the normal distribution function at a confidence level of 95% which were shown in Figure 6.

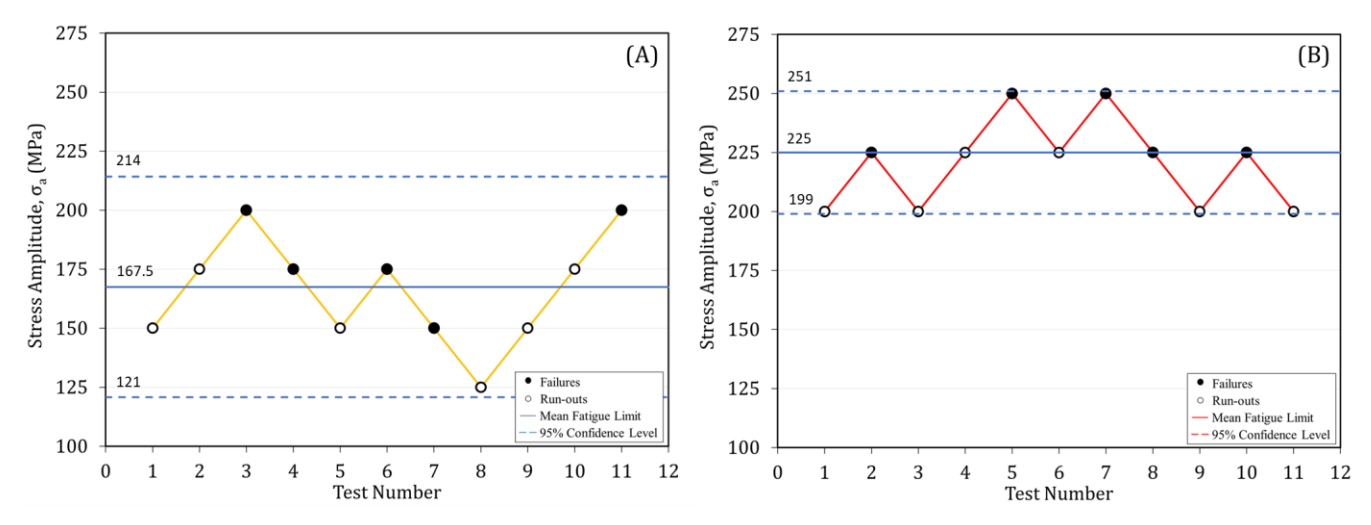


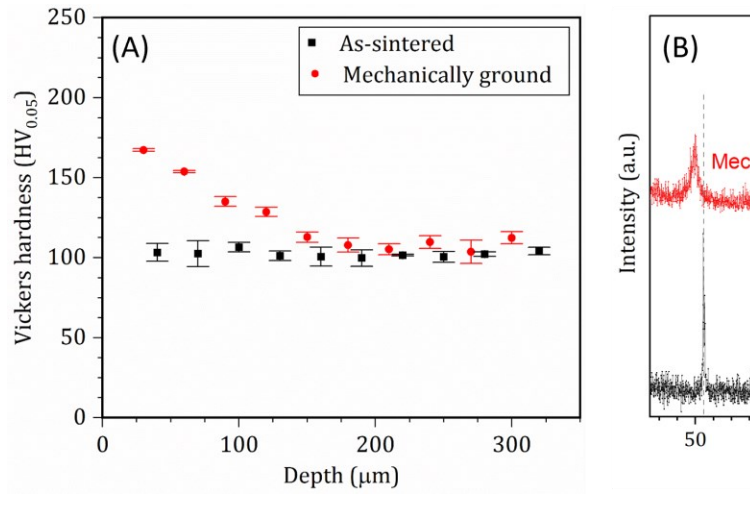
Figure 6. Staircase test results for the (A) as-sintered and (B) mechanically polished binder jetted 316L SS specimens.

The results indicated that the fatigue endurance limit of the as-sintered binder jetted parts was lower compared to the mechanically ground specimens. Specifically, the mean fatigue limit for the as-sintered parts was around 168 MPa, while it increased to 225 MPa after mechanical grinding. The fatigue limit values for L-PBF processed 316L SS parts were specified in [38] to be ~170 MPa (as-built) and 190 MPa (mechanically ground) at R_{σ} =-1. Another study utilizing the L-PBF manufacturing technique reported a fatigue limit value of 250 MPa [35]. These results showed that the fatigue limit values for L-PBF parts fell within the range of specification limits obtained for the binder jetted specimens. Kumar et al. [20] reported similar observations in their comparison of rotary bending fatigue performance of the binder jetted and L-PBF processed parts. Their experiments on the L-PBF samples showed that the unlimited fatigue lifetime was obtained in the stress range of 101-175 MPa, which was relatively low compared to the specimens processed via binder jetting. The elongation of the binder jetted 316L SS was reported to be 90% when sintered at 1400°C for 2 h [28]. In contrast, this value ranged between 30-70% for L-PBF processed 316L SS [45,46]. Therefore, the fatigue lifetime at relatively low stress levels seems to be influenced by strain hardening rather than the level of porosity. Any reduction in strain hardening of 316L SS may negatively impact ductility, thus lowering the fatigue performance in low-stress ranges.

3.4. Effect of mechanical grinding on sub-surface deformation and incuded stress

The Vickers microhardness test results, depicted in Figure 7(A), revealed that the hardness in the subsurface region was approximately $105\pm6~HV_{0.05}$ for both samples. It was unsurprising that no changes in hardness values were observed from the edge towards the center of the cross-section in the as-sintered specimen. Conversely, the mechanically ground part displayed an increasing trend in the hardness values starting from around $125~\mu m$ from the surface, reaching a maximum of $167~HV_{0.05}$ close to the edge. This implies the presence of extensive work hardening in the 316L~SS alloy caused by the mechanical grinding process, which may have induced compressive stress, ultimately improving the fatigue properties. Similar observations were reported in a study by [24] on the surface-treated 625 alloy fabricated via binder jetting.

X-ray diffraction analysis was used to quantify the induced stress on the surface of the mechanically ground specimens and to compare it with the as-sintered parts. The results of this analysis are presented in Figure 7(B). Two main differences were observed between the as-sintered and ground surface conditions: (1) all peaks shifted to lower 2θ values, and (2) peak broadening occurred. According to Bragg's law [47], the shift in peak position in the mechanically ground surface condition of binder jetted alloy resulted in an increase in out-of-plane d-spacing values, as demonstrated by Mostafaei et al. [24]. The broadening of the peaks could be attributed to grain refinement and broader micro-strain variations. Therefore, the surface treatment may improve the fatigue lifetime, as shown in previous studies [48,49].



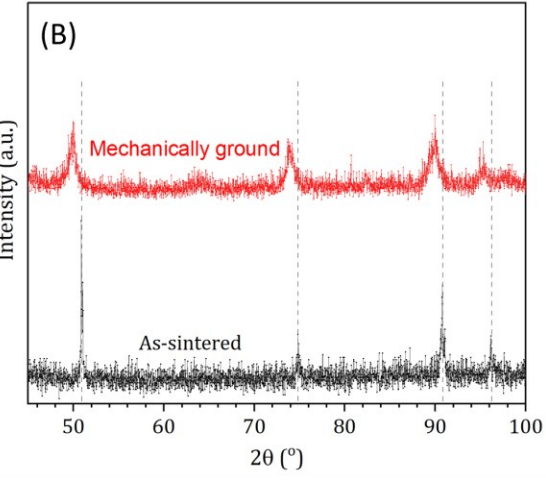


Figure 7. (A) Microhardness measurements as a function of depth below the surface of the sample and (B) X-ray diffraction pattern taken from the curved surface of the binder jetted 316L SS specimens in an as-sintered and mechanically ground conditions.

3.5. Fractography and deformation history analysis

The fracture surfaces of both the as-sintered and mechanically ground 316L SS specimens, which were subjected to different stress amplitudes, were analyzed and the results are presented in Figure 8. The fracture surfaces were observed to have three distinct regions: crack initiation, crack propagation, and final fracture sites. The white arrows in the low-magnification micrographs indicated that cracks were initiated from the surface of the fatigue specimens regardless of the surface condition and stress level. However, the number of crack initiation sites increased with increasing stress level. Due to the layer-wise printing process of binder jetting and the effect of binder hit on the powder bed, a higher number of crack initiation sites were observed on the as-sintered surface specimens compared to the mechanically ground specimens. Dash-line curves on the low-magnification optical micrographs were used to approximately identify the transition from crack growth regions to final fracture areas. It was found that with decreasing stress level, the area associated with crack propagation increased in size, dominating the fracture mechanism and resulting in a smaller final fracture region. Furthermore, the transition from the fatigue crack growth region to the final fracture area was accompanied by a gradual decrease in the surface area, resulting in an increase in stress intensity.

SEM micrographs were captured at higher magnification in two distinct regions, namely crack propagation and final fracture, as illustrated in Figure 8. In ductile materials, the failure mechanism at the fatigue crack propagation site is often characterized by a pattern of ripples referred to as fatigue striations that are responsible for advancing the crack front. As shown in Figure 8, such a striation pattern was evident, indicating crack growth perpendicular to the loading direction. Furthermore, the distance between the striation marks varied in the high magnification micrographs of different stress amplitudes for both surface conditions. The average distance between the microscopic striation marks in the crack propagation sites was determined and reported in

Table 1. The results indicated that as the stress amplitude increased, the space between the striation marks also increased. This information can aid in the failure analysis of parts subjected to cyclic loading since the number and distance between such marks can provide an estimate of the lifetime of the failed part. In the final fracture site, the fracture mechanism was dominated by ductile dimple failures, which were organized by micro-void coalescence (MVC), indicating the ductile behavior of the binder jetted 316L SS. Muhammad et al. [27]also reported similar ductile dimple features within the final fracture region for samples subjected to loading, where the final fracture area was reduced, leading to final failure by the formation of small shear slips.

Under fatigue loading, fatigue cracks could nucleate at or near material discontinuities including second-phase particles, grain boundaries, twin boundaries, pores, voids, as well as slip bands. In an earlier work by Jamalkhani et al. [28], it was shown that the binder jetted 316L SS sintered at 1400 °C for 2 h had a relative bulk density (ρ_{bulk}) of 99.4% and an apparent bulk density (ρ_{app}) of 99.7%. There are ~0.6% pores in the sintered part (1- ρ_{bulk}); nonetheless, the difference between ho_{app} and ho_{bulk} provides the percentage of open-tosurface pores (~0.3%). This is critical for parts subjected to cyclic loading in which open-tosurface pores act as stress concentration zones leading to common sites for microcracks to nucleate. Fatigue results in section 3.3 showed that the mechanical grinding could enhance the HCF response of the binder jetted 316L SS parts, specifically at higher stress levels, by removing open-to-surface pores (with less than 0.3% in the population) as well as minimizing surface roughness to values below $R_a = 0.21 \mu m$. However, at relatively low stress levels, a slight improvement was seen in fatigue performance after the surface treatment. In fact, the influence of the polished surface, which brought the low surface roughness condition to the binder jetted 316L SS, was more pronounced at short lives (N_f < 10³–10⁴) since the crack(s) initiated early during the fatigue test due to the relatively high stress amplitudes.

Table 3. Average distance of striation marks in the crack propagation area of the fractured binder jetted 316L SS specimens.

Surface condition	Average distance of striation mark [µm] under the applied stress aplitude [MPa]						
	200	225	250	275	300	325	
As-sintered	0.51±0.02	0.62±0.10	0.80±0.10	3.56±0.30	-	-	
Mechanically ground	-	0.78±0.01	0.79±0.09	2.80±0.32	3.15±0.28	3.17±0.34	

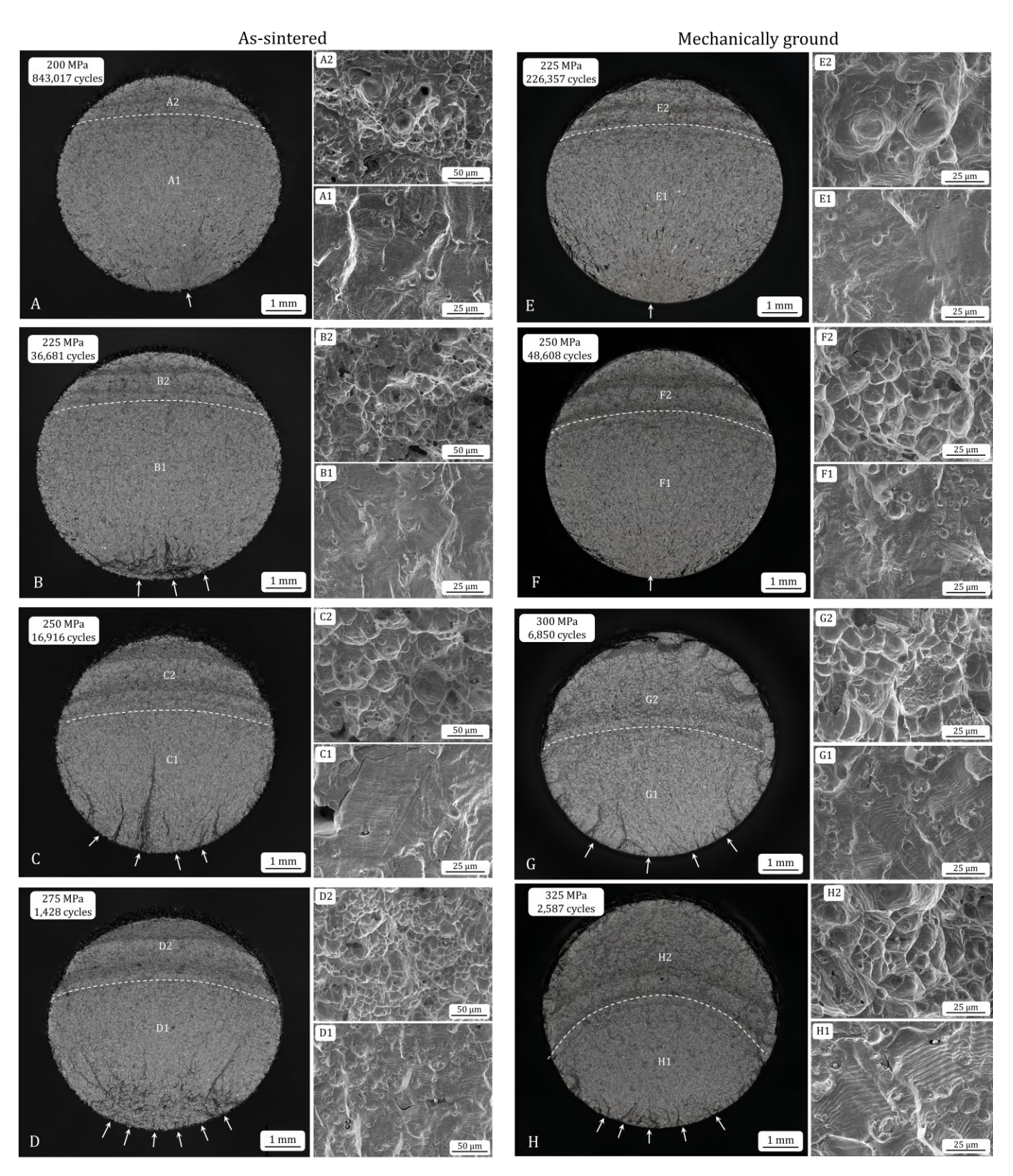


Figure 8. Fracture surfaces of the (left) as-sintered and (right) mechanically ground binder jetted 316L SS fatigue specimens subjected to stress amplitudes ranging between 200-275 MPa (for as-sintered) and 225-325 MPa (for mechanically ground).

The OM micrograph of the sliced fracture surface, post-experiment EBSD, and the SEM micrographs were investigated on selected specimens at low and high stress levels in the assintered and mechanically ground conditions whose results were shown in Figure 9 and Figure 10, respectively. In Figure 9(left), the fracture surface of the as-sintered part subjected to a stress amplitude of 200 MPa appeared flat from the side view. When the stress amplitude was >200 MPa, the fracture surface was found to be uneven in both surface conditions. In Figure 9(right) at 200 MPa, the crack initiation site was found to be concentrated in one single spot at the fracture surface which is typically detected at low stress levels. In contrast, at a relatively high stress level of 275 MPa, such an initiation site offered multiple crack nucleation spots along with noticeable ratcheting marks moving parallel to the direction of crack propagation in which activation and accumulation of plastic strain occurred [50]. Similar observations could be seen in Figure 10 for the mechanically ground condition.

The investigation of the material strain history in austenitic steel subjected to localized deformation can be conveniently carried out by EBSD mapping [51]. Therefore, EBSD datasets were recorded at three different locations including crack initiation, crack propagation, and the final fracture and are presented in Figure 9 and Figure 10 to analyze the failure modes in binder jetted 316L SS. The IPF map in the EBSD datasets showed equiaxed grain orientation containing annealing twins in the crack initiation and propagation sites (A1 and A2), while partially elongated FCC grains were visible in the final fracture zone (A3). The KAM map, which measures changes in the local misorientation caused by geometrically necessary dislocations [52], revealed almost no misorientation gradients in the crack initiation site in zone A1, indicating that excess deformation was still in its elastic stage. However, as the crack propagated, the strain gradient became apparent at the grain boundaries, delta-ferrite phase, and porosities, which all acted as discontinuities in the microstructure of the binder jetted 316L SS. Notably, there were no significant gradients inside the grains at this stage. Moreover, the fracture mechanism in this region (A2) was found to be fatigue striations that relied on the cyclic nature of fatigue (see Figure 8). In the final fracture area (A3), the localized plasticity culminated, resulting in an increased local density of dislocations, with dimple features being the dominant fracture mechanism. These dimple marks are typically observed when the material undergoes plastic deformation, where MVC occurs due to nucleation, growth, and coalescence of micro-voids. The MVC is usually considered a high-energy process that occurs at high crack growth rates and is established in the final fracture areas [40]. Finally, the dense network of slip lines apparent in A3 zones is related to the low stacking fault energy (i.e., between 15-45 mJ/m²) of 316L SS [53].

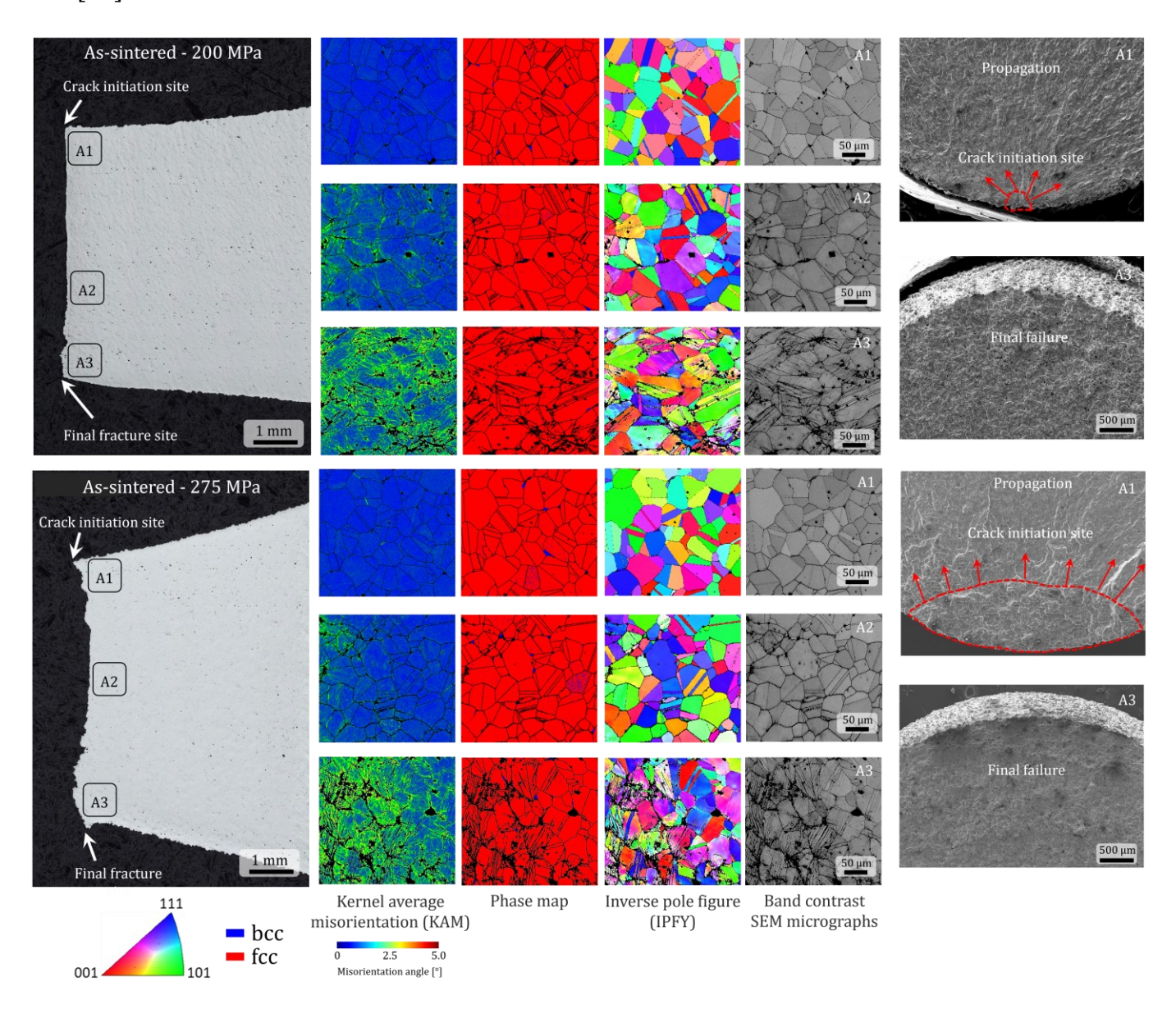


Figure 9. Microscopy observations on the fracture surface of as-sintered binder jetted 316L SS specimen. Two stress amplitudes were selected for imaging. (left) Optical micrographs at the cross-section of the fatigue samples showing three selected areas for EBSD analysis including (A1) crack initiation, (A2) propagation, and (A3) final failure. (middle) Microstructure analysis using EBSD: kernel average misorientation (KAM) maps on the cross-section of the specimen, phase maps, inverse pole figure (IPF-Y) maps, and band contrast SEM micrographs. (right) Fatigue fracture surfaces indicating crack initiation zone using red dash line. Red arrows showed the crack growth directions.

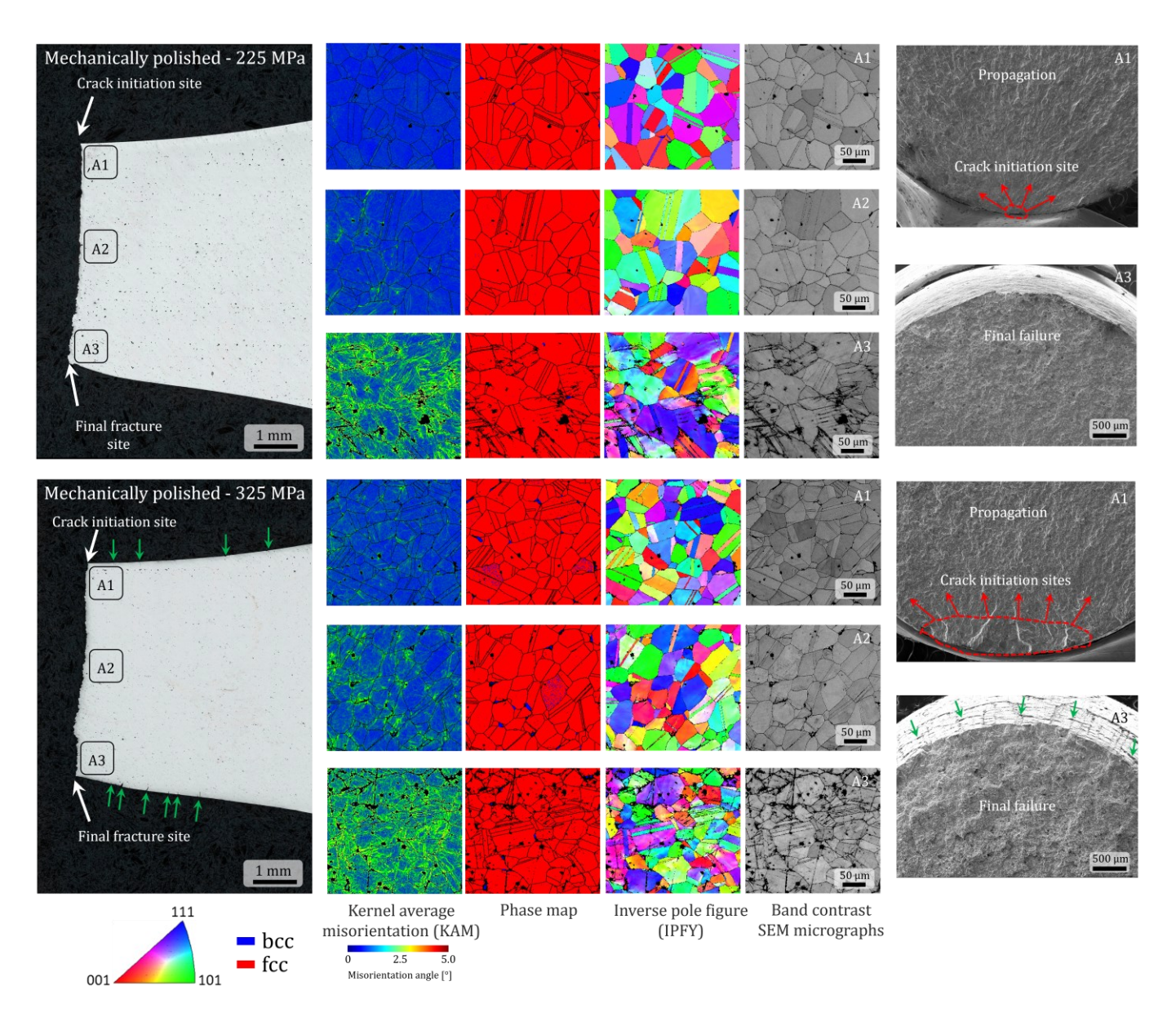


Figure 10. Microscopy observations on the fracture surface of mechanically ground binder jetted 316L SS specimen. Two stress amplitudes were selected for imaging. (left) Optical micrographs at the cross-section of the fatigue samples showing three selected areas for EBSD analysis including (A1) crack initiation, (A2) propagation, and (A3) final failure. (middle) Microstructure analysis using EBSD: kernel average misorientation (KAM) maps on the cross-section of the specimen, phase maps, inverse pole figure (IPF-Y) maps, and band contrast SEM micrographs. (right) Fatigue fracture surfaces indicating crack initiation zone using red dash line. Red arrows showed the crack growth directions. Green arrows showed the formation of surface cracks due to plastic deformation.

High magnification SEM micrographs taken from the fracture surface of the as-sintered specimens (Figure 9, right) indicated that cracks initiated on the surface due to the high surface roughness. As discussed in Section 3.2 and in our earlier work [28], print lines cannot

be avoided in binder jetted specimens, and they remain on the surface even after sintering. Additionally, the curvature on the fatigue samples added more steps and roughness to the as-sintered samples, which played a role in crack initiation from surface defects. However, two different behaviors were observed when the parts were mechanically ground. At a stress value of 225 MPa, a single subsurface crack initiation site was observed on the fracture surface (see Figure 10, right). This implies that at low-stress regimes, the presence of compressive stress on the sample surface (mainly) and the reduction of surface roughness transfer crack initiation sites from the surface to subsurface. However, at higher stress levels (i.e., 325 MPa), where partial plastic deformation occurs on the sample (see KAM map in A1 region), cracks were evident on the curved surface (green arrows). Thus, these newly developed surface defects played the role of an initial site for crack initiation. In other words, although the mechanically ground specimen showed residual compressive stresses up to 125 um beneath the surface (as evident by hardness measurement), the applied stress level was well beyond the yielding stress (202 MPa [28]), and the material was plastically deformed, leaving microcracks on the surface. Selected samples at higher magnifications are shown in Figure 11 in support of the given discussions.

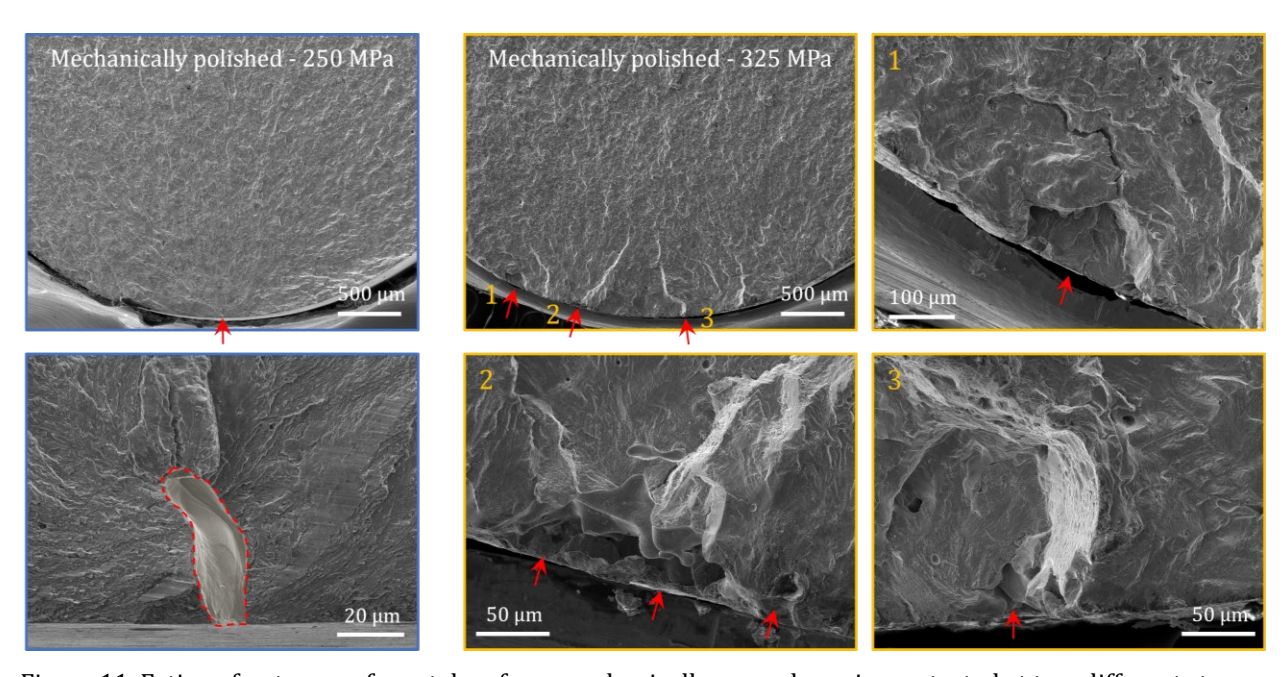


Figure 11. Fatigue fracture surfaces taken from mechanically ground specimens tested at two different stress leves. Subsurface defect was evident at lower stress values, while surface cracking due to plastic deformation resulted in crack initiation at the surface.

4. Conclusion

In this study, the high-cycle fatigue properties of the binder jetted fine 316L SS powder subjected to axial tensile loading was investigated in the as-sintered and mechanically ground surface conditions. Obtained results are as follows:

- Microstructure observations using SEM and EBSD revealed the formation of equiaxed austenite grains with a grain size of approximately 33 μ m, along with a trace amount of delta-ferrite at the grain boundaries. Computed tomography analysis confirmed a relative density of 99.8% in the binder jetted 316L SS specimens that were sintered at 1400 °C for 2 h.
- The surface roughness analysis showed that the as-sintered surface had an average roughness of R_a =6.56±0.58 µm while it was reduced to R_a =0.21±0.03 µm after mechanical grinding. Such a ~97%-decline in the surface roughness led to a reduction in crack initiation sites, thereby improving fatigue life.
- The results obtained from the S-N curve and regression analysis indicated a superior fatigue response in the mechanically ground surface condition, particularly at high stress amplitudes where $N_f < 10^3 10^4$. The fatigue endurance limit analysis revealed a mean fatigue limit of approximately 168 MPa in the as-sintered parts and 225 MPa after mechanical grinding. The remarkable performance in the fatigue endurance limit of binder jetted 316L SS can be attributed to its strain hardening compared to 316L SS manufactured by other techniques.
- Hardness and X-ray diffraction analyses showed that mechanical grinding created an in-plane compressive residual stress in the top $\sim 125~\mu m$ layer of the post-processed specimens, resulting in an enhanced fatigue performance.
- Fractography revealed that the number of crack initiation sites on the fracture surface of the as-sintered specimens was higher than that of mechanically ground specimens due to the presence of surface micro-notches. Additionally, cracks were observed to initiate at the surface of the as-sintered specimens irrespective of the applied stress level. In contrast, the mechanically ground samples showed no evidence of crack initiation from the surface at low stress levels, where subsurface defects were responsible for initiating cracks. However, at stress levels much higher than the yield

- stress, plastic deformation resulted in the formation of surface cracks, which led to crack initiation at the surface.
- The fracture behavior of the binder jetted 316L SS in both surface conditions was found to be similar. Both conditions exhibited a flat fracture surface with striation marks in the crack propagation region, and dimple features in the final fracture region. EBSD analysis on the cross-sections near the fracture surface revealed that the crack initiation sites had strain-free equiaxed grains, while the crack propagation and final fracture regions showed evidence of higher plastic deformation rates due to the presence of high local density of dislocations. This was reflected by the increased misorientation gradients in the kernel average misorientation maps.

Acknowledgements

AM would like to acknowledge the startup funding from the Department of Mechanical, Materials and Aerospace Engineering and Armour College of Engineering at Illinois Institute of Technology at Chicago, Illinois. Also, partial support from the National Science Foundation under grant number DMR-2050916 is appreciated by all authors.

References

- [1] ISO/ASTM DIS 52900 Additive manufacturing General principles Fundamentals and vocabulary, (2020).
- [2] A. Mostafaei, A.M. Elliott, J.E. Barnes, C.L. Cramer, P. Nandwana, M. Chmielus, Binder jet 3D printing process parameters, materials, properties, modeling, and challenges, Prog. Mater. Sci. 119 (2021) 100707.
- [3] C.L. Cramer, A.M. Elliott, J.O. Kiggans, B. Haberl, D.C. Anderson, Processing of complex-shaped collimators made via binder jet additive manufacturing of B 4 C and pressureless melt in filtration of Al ★, Mater. Des. 180 (2019) 107956.
- [4] L. Li, B. Post, V. Kunc, A.M. Elliott, M.P. Paranthaman, Additive manufacturing of nearnet-shape bonded magnets: Prospects and challenges, Scr. Mater. 135 (2017) 100–104.
- [5] A. Mostafaei, E.L. Stevens, J.J. Ference, D.E. Schmidt, M. Chmielus, Binder jetting of a complex-shaped metal partial denture framework, Addit. Manuf. 21 (2018) 63–68.
- [6] C.L. Cramer, P. Nandwana, J. Yan, S.F. Evans, A.M. Elliott, C. Chinnasamy, M.P.

- Paranthaman, Binder jet additive manufacturing method to fabricate near net shape crack-free highly dense Fe-6.5 wt.% Si soft magnets, Heliyon. 5 (2019) e02804.
- [7] E. Martin, A. Natarajan, S. Kottilingam, R. Batmaz, Binder jetting of "Hard-to-Weld" high gamma prime nickel-based superalloy RENÉ 108, Addit. Manuf. 39 (2021) 101894.
- [8] D. Huber, L. Vogel, A. Fischer, The Effects of Sintering Temperature and Hold Time on Densification, Mechanical Properties and Microstructural Characteristics of Binder Jet 3D Printed 17-4 PH Stainless Steel, Addit. Manuf. (2021) 102114.
- [9] C. Zheng, A. Mostafaei, P.R. de Vecchis, I. Nettleship, M. Chmielus, Microstructure evolution for isothermal sintering of binder jet 3D printed alloy 625 above and below the solidus temperature, Addit. Manuf. 47 (2021) 102276.
- [10] A. Mostafaei, J. Toman, E.L. Stevens, E.T. Hughes, Y.L. Krimer, M. Chmielus, Microstructural evolution and mechanical properties of differently heat-treated binder jet printed samples from gas- and water-atomized alloy 625 powders, Acta Mater. 124 (2017) 280–289.
- [11] E. Wheat, M. Vlasea, J. Hinebaugh, C. Metcalfe, Sinter structure analysis of titanium structures fabricated via binder jetting additive manufacturing, Mater. Des. 156 (2018) 167–183.
- [12] A. Mostafaei, P. Rodriguez De Vecchis, E.L. Stevens, M. Chmielus, Sintering regimes and resulting microstructure and properties of binder jet 3D printed Ni-Mn-Ga magnetic shape memory alloys, Acta Mater. 154 (2018).
- [13] M. Ziaee, E.M. Tridas, N.B. Crane, Binder-Jet Printing of Fine Stainless Steel Powder with Varied Final Density, Jom. 69 (2017) 592–596.
- [14] C.L. Cramer, P. Nandwana, R.A. Lowden, A.M. Elliott, Infiltration studies of additive manufacture of WC with Co using binder jetting and pressureless melt method, Addit. Manuf. 28 (2019) 333–343.
- [15] A. Mostafaei, P.R. De Vecchis, K.A. Kimes, D. Elhassid, M. Chmielus, Effect of binder saturation and drying time on microstructure and resulting properties of sinter-HIP binder-jet 3D-printed WC-Co composites, Addit. Manuf. 46 (2021) 102128.
- [16] H. Miyanaji, N. Momenzadeh, L. Yang, Effect of printing speed on quality of printed parts in Binder Jetting Process, Addit. Manuf. 20 (2018) 1–10.
- [17] H. Miyanaji, D. Ma, M.A. Atwater, K.A. Darling, V.H. Hammond, C.B. Williams, Binder Jetting Additive Manufacturing of Copper Foam Structures, Addit. Manuf. 32 (2020) 100960.
- [18] A. Mostafaei, E. Stevens, E. Hughes, S. Biery, C. Hilla, M. Chmielus, Powder bed binder jet printed alloy 625: densification, microstructure and mechanical properties, Mater. Des. 108 (2016) 126–135.
- [19] A. Mostafaei, Y. Behnamian, Y.L. Krimer, E.L. Stevens, J.L. Luo, M. Chmielus, Effect of solutionizing and aging on the microstructure and mechanical properties of powder bed binder jet printed nickel-based superalloy 625, Mater. Des. 111 (2016) 482–491.

- [20] P. Kumar, R. Jayaraj, J. Suryawanshi, U.R. Satwik, J. McKinnell, U. Ramamurty, Fatigue strength of additively manufactured 316L austenitic stainless steel, Acta Mater. 199 (2020) 225–239.
- [21] M. Salehi, H.L. Seet, M. Gupta, H. Farnoush, S. Maleksaeedi, M.L.S. Nai, Rapid densification of additive manufactured magnesium alloys via microwave sintering, Addit. Manuf. 37 (2021) 140353.
- [22] M. Salehi, S. Maleksaeedi, S.M.L. Nai, G.K. Meenashisundaram, M.H. Goh, M. Gupta, A paradigm shift towards compositionally zero-sum binderless 3D printing of magnesium alloys via capillary-mediated bridging, Acta Mater. 165 (2019) 294–306.
- [23] D. Huber, P. Stich, A. Fischer, Heat Treatment of 17 4 PH Stainless Steel Produced by Binder Jet Additive Manufacturing (BJAM) from N 2 Atomized Powder, Prog. Addit. Manuf. (2021).
- [24] A. Mostafaei, S.H.V.R. Neelapu, C. Kisailus, L.M. Nath, T.D.B. Jacobs, M. Chmielus, Characterizing surface finish and fatigue behavior in binder-jet 3D-printed nickel-based superalloy 625, Addit. Manuf. 24 (2018) 200–209.
- [25] J. Radhakrishnan, P. Kumar, S.S. Gan, A. Bryl, J. McKinnell, U. Ramamurty, Fatigue resistance of the binder jet printed 17-4 precipitation hardened martensitic stainless steel, Mater. Sci. Eng. A. 865 (2023) 144451.
- [26] K. Kimes, K. Myers, A. Klein, M. Ahlfors, E. Stevens, M. Chmielus, Binder Jet 3D Printing of 316L Stainless Steel: Effects of HIP on Fatigue, Microsc. Microanal. 25 (2019) 2600–2601.
- [27] W. Muhammad, R. Batmaz, A. Natarajan, E. Martin, Effect of binder jetting microstructure variability on low cycle fatigue behavior of 316L, Mater. Sci. Eng. A. 839 (2022) 142820.
- [28] M. Jamalkhani, M. Asherloo, O. Gurlekce, I.-T. Ho, M. Heim, D. Nelson, A. Mostafaei, Deciphering microstructure-defect-property relationships of vacuum-sintered binder jetted fine 316L austenitic stainless steel powder, Addit. Manuf. (2022).
- [29] A. Mostafaei, P. Rodriguez De Vecchis, I. Nettleship, M. Chmielus, Effect of powder size distribution on densification and microstructural evolution of binder-jet 3D-printed alloy 625, Mater. Des. 162 (2019) 375–383.
- [30] M.J. Khameneh, M. Azadi, Reliability prediction, scatter-band analysis and fatigue limit assessment of high-cycle fatigue properties in EN-GJS700-2 ductile cast iron, (n.d.).
- [31] N. Lecis, M. Mariani, R. Beltrami, L. Emanuelli, R. Casati, M. Vedani, A. Molinari, Effects of process parameters, debinding and sintering on the microstructure of 316L stainless steel produced by binder jetting, Mater. Sci. Eng. A. 828 (2021) 142108.
- [32] S. Mirzababaei, B.K. Paul, S. Pasebani, Microstructure-property relationship in binder jet produced and vacuum sintered 316 L, Addit. Manuf. 53 (2022) 102720.
- [33] A.C. Rios, E. Hryha, E. Olesvsky, P. Harlin, Sintering anisotropy of binder jetted 316L stainless steel: part II microstructure evolution during sintering, Powder Metall.

- (2022).
- [34] B.P. Kashyap, K. Tangri, Grain growth behaviour of type 316L stainless steel, Mater. Sci. Eng. A. 149 (1992) 13–16.
- [35] R. Shrestha, J. Simsiriwong, N. Shamsaei, Fatigue behavior of additive manufactured 316L stainless steel under axial versus rotating-bending loading: Synergistic effects of stress gradient, surface roughness, and volumetric defects, Int. J. Fatigue. 144 (2021) 106063.
- [36] N. Kurgan, R. Varol, Mechanical properties of P/M 316L stainless steel materials, Powder Technol. 201 (2010) 242–247.
- [37] Y. Zhang, E. Feng, W. Mo, Y. Lv, R. Ma, S. Ye, X. Wang, P. Yu, On the microstructures and fatigue behaviors of 316L stainless steel metal injection molded with gas-and water-atomized powders, Metals (Basel). 8 (2018).
- [38] A.B. Spierings, T.L. Starr, K. Wegener, Fatigue performance of additive manufactured metallic parts, Rapid Prototyp. J. 19 (2013) 88–94.
- [39] T. Łagoda, S. Vantadori, K. Głowacka, M. Kurek, K. Kluger, Using the Smith-Watson-Topper Parameter and Its Modifications to Calculate the Fatigue Life of Metals: The State-of-the-Art, Materials (Basel). 15 (2022).
- [40] R. Stephens, A. Fatemi, R.R. Tephens, H. Fuchs, METAL FATIGUE Second Edition, 2001.
- [41] Y.-L. Lee, Fatigue testing and analysis: theory and practice, (2005).
- [42] Fatigue ASM International, Elements of Metallurgy and Engineering Alloys, Chapter 14 (2008) 243–265.
- [43] P.D. Enrique, E. Marzbanrad, Y. Mahmoodkhani, Z. Jiao, E. Toyserkani, N.Y. Zhou, Surface modification of binder-jet additive manufactured Inconel 625 via electrospark deposition, Surf. Coatings Technol. 362 (2019) 141–149.
- [44] N. Huang, O.J. Cook, R.L.W. Smithson, C.M. Kube, A.P. Argüelles, A.M. Beese, Use of ultrasound to identify microstructure-property relationships in 316 stainless steel fabricated with binder jet additive manufacturing, Addit. Manuf. 51 (2022) 102591.
- [45] X. Wang, J.A. Muñiz-Lerma, O. Sánchez-Mata, M. Attarian Shandiz, M. Brochu, Microstructure and mechanical properties of stainless steel 316L vertical struts manufactured by laser powder bed fusion process, Mater. Sci. Eng. A. 736 (2018) 27-40.
- [46] M. Khorasani, A.H. Ghasemi, U.S. Awan, S. Singamneni, G. Littlefair, E. Farabi, M. Leary, I. Gibson, J.K. Veetil, B. Rolfe, On the role of process parameters on meltpool temperature and tensile properties of stainless steel 316L produced by powder bed fusion, J. Mater. Res. Technol. 12 (2021) 2438–2452.
- [47] S. Dai, Y. Zhu, Z. Huang, Microstructure evolution and strengthening mechanisms of pure titanium with nano-structured surface obtained by high energy shot peening, Vacuum. 125 (2016) 215–221.

- [48] O. Unal, R. Varol, Surface severe plastic deformation of AISI 304 via conventional shot peening, severe shot peening and repeening, Appl. Surf. Sci. 351 (2015) 289–295.
- [49] O. Unal, E. Maleki, R. Varol, Effect of severe shot peening and ultra-low temperature plasma nitriding on Ti-6Al-4V alloy, Vacuum. 150 (2018) 69–78.
- [50] M. Zhang, C.N. Sun, X. Zhang, J. Wei, D. Hardacre, H. Li, High cycle fatigue and ratcheting interaction of laser powder bed fusion stainless steel 316L: Fracture behaviour and stress-based modelling, Int. J. Fatigue. 121 (2019) 252–264.
- [51] M.N. Gussev, K.J. Leonard, In situ SEM-EBSD analysis of plastic deformation mechanisms in neutron-irradiated austenitic steel, J. Nucl. Mater. 517 (2019) 45–56.
- [52] M. KAMAYA, K. KUBUSHIRO, Y. SAKAKIBARA, S. SUZUKI, H. MORITA, R. YODA, D. KOBAYASHI, K. YAMAGIWA, T. NISHIOKA, Y. YAMAZAKI, Y. KAMADA, T. HANADA, T. OHTANI, Round robin crystal orientation measurement using EBSD for damage assessment, Mech. Eng. J. 3 (2016) 16-00077-16-00077.
- [53] S. Kibey, J.B. Liu, D.D. Johnson, H. Sehitoglu, Predicting twinning stress in fcc metals: Linking twin-energy pathways to twin nucleation, Acta Mater. 55 (2007) 6843–6851.